



# Effect of Fe on the photocatalytic removal of NO<sub>x</sub> over visible light responsive Fe/TiO<sub>2</sub> catalysts

Jinzhu Ma, Hong He\*, Fudong Liu<sup>1</sup>

State Key Joint Laboratory of Environment Simulation and Pollution Control, Research Center for Eco-Environmental Sciences, Chinese Academy of Sciences, Beijing 100085, China



## ARTICLE INFO

### Article history:

Received 12 March 2015

Received in revised form 24 April 2015

Accepted 1 May 2015

Available online 5 May 2015

### Keywords:

Fe/TiO<sub>2</sub>

Visible light

Photocatalysis

NO removal

DFT

## ABSTRACT

We synthesized different Fe/TiO<sub>2</sub> catalysts and studied the influence of Fe on the structure and performance of Fe/TiO<sub>2</sub> as a photocatalyst to remove gaseous NO in air under visible light. The electron paramagnetic resonance results revealed that Fe ions substituted the Ti ions of TiO<sub>2</sub> prepared by co-precipitation and homogeneous precipitation method. More Fe ions were incorporated into the crystal lattice of TiO<sub>2</sub> prepared by co-precipitation method than that prepared by homogeneous precipitation method. No Fe ions were incorporated into the crystal lattice of TiO<sub>2</sub> prepared by conventional wet impregnation method. Furthermore, Fe doping influenced the UV-vis absorption and photoluminescence of TiO<sub>2</sub>. The higher photocatalytic activity of Fe/TiO<sub>2</sub> prepared by co-precipitation method was attributed to the synergistic effects of more visible light absorption and minimum electron hole recombination caused by the Fe ions incorporated into the crystal lattice of TiO<sub>2</sub>. Density functional theory calculations further confirmed the role of Fe on the electronic structure of TiO<sub>2</sub>.

© 2015 Elsevier B.V. All rights reserved.

## 1. Introduction

Nitrogen oxides (NO<sub>x</sub>), mainly produced from combustion of fossil fuels, are considered as a major contributors to atmospheric environmental problems, such as urban haze, photochemical smog, acid rain, and so on [1,2]. NO<sub>x</sub> concentration in the atmosphere has greatly increased over the past few decades because of the increased number of coal burning, motor vehicles, and industrial emission [1]. The conventional approaches, such as selective catalytic reduction (SCR), wet scrubbing, adsorption, biofiltration, and catalytic decomposition can remove NO<sub>x</sub> from emission sources; however, they are not economically feasible for the removal of NO at parts per billion (ppb) levels in urban environments [3,4]. Semiconductor photocatalysis, as a “green” technology, which utilize natural sunlight to purify air pollutants of low concentration at ambient conditions, has been used to remove NO<sub>x</sub> [5–13].

Since the discovery of photocatalytic splitting of water on a titanium dioxide (TiO<sub>2</sub>) electrode in 1972 [14], TiO<sub>2</sub> has long been a promising candidate for photocatalysis applications due to its strong photocatalytic oxidation performance, photostability,

natural abundance, and nontoxicity [15]. However, the relatively large band gap of TiO<sub>2</sub> (3.0–3.2 eV) limits its application in the visible light region (400 nm < λ < 750 nm), which accounts for 43% of incoming solar energy [3,16]. Therefore, developing visible light-responsive photocatalysts with high efficiency and stability are desirable and has become one of the most important topics in environmental photocatalysis [17,18]. Metal/nonmetal elements doping, narrower band gap semiconductor coupling, hydrogen treatment and photosensitization with dyes have been applied to enhance the visible light activity of TiO<sub>2</sub> [19–27].

Metal element doping is one of the typical approaches to extend the spectral response of TiO<sub>2</sub> to the visible-light region. Some metal elements, such as Fe, V, Co, Mo and Cr have been employed to tune the electronic structure and enhance the photocatalytic activity of TiO<sub>2</sub> [21,28–32]. Among these elements, Fe has attracted special attention as the ionic radius of Fe<sup>3+</sup>(0.64 Å) is similar to that of Ti<sup>4+</sup>(0.68 Å), resulting in easier insertion of Fe<sup>3+</sup> into the crystal structure of TiO<sub>2</sub> [33]. As a dopant, however, the role of Fe<sup>3+</sup> is still controversial. Some authors have suggested that the detrimental effect of Fe<sup>3+</sup> as a promoter increases the rate of charge recombination, while other authors have reported on the beneficial effects of Fe<sup>3+</sup> in the separation of photogenerated electrons and holes and in the shift of the absorption edge into the visible-light range with the narrowing of the band gap, thus increasing photocatalytic activity [31,34,35]. It is known that the role of Fe is determined by doping levels. The solubility limit of Fe in TiO<sub>2</sub> is

\* Corresponding author. Tel.: +86 10 62849123; fax: +86 10 62849123.

E-mail address: [honghe@rcees.ac.cn](mailto:honghe@rcees.ac.cn) (H. He).

<sup>1</sup> Present address: Materials Sciences Division, Lawrence Berkeley National Laboratory, 1 Cyclotron Road, Berkeley, CA 94720, United States.

1.0%, with separate  $\alpha$ -Fe<sub>2</sub>O<sub>3</sub> or Fe<sub>2</sub>TiO<sub>5</sub> phases forming above this limit [36]. A separate Fe<sub>2</sub>O<sub>3</sub> phase is detrimental to oxygen activation and photocatalytic activity [35]. Therefore, high Fe doping levels may decrease photocatalytic activity. On the other hand, surface or bulk doping may also influence the role of Fe. It is difficult for photogenerated holes or electrons trapped at bulk-doped Fe ions to migrate to the surface without recombination [37]. Experimental and theoretical computation results suggest that Fe ions on the surface may increase photocatalytic activity, while Fe ions in bulk may have a negative effect [37].

Although the state of Fe has great influence on photocatalytic activity, it has not been systematically investigated. We synthesized different Fe/TiO<sub>2</sub> catalysts and studied the influence of Fe on the structure and performance of Fe/TiO<sub>2</sub> as a photocatalyst to remove gaseous NO in air under visible light.

## 2. Experimental

### 2.1. Materials preparation

The Fe/TiO<sub>2</sub> catalysts were synthesized by facile co-precipitation method using Fe(NO<sub>3</sub>)<sub>3</sub>•9H<sub>2</sub>O ( $\geq 98.5\%$ ) as a Fe precursor and Ti(SO<sub>4</sub>)<sub>2</sub> ( $\geq 96\%$ ) as a Ti precursor (the molar content of Fe was 0.1%, 0.3%, 0.5%, 0.7% and 1%) and 25 wt% NH<sub>3</sub>•H<sub>2</sub>O as precipitator. After the pH of the mixed solution rose to 10 in the co-precipitation process, the precipitate cakes were first filtrated and washed by distilled water, and then desiccated at 100 °C for 12 h and calcined at 400 °C for 6 h under air conditions (the heating rate kept at 5 °C/min). The catalysts was signified by Fe<sub>x</sub>%T (x means the molar content of Fe). Pristine Fe<sub>2</sub>O<sub>3</sub> and TiO<sub>2</sub> were synthesized using Fe(NO<sub>3</sub>)<sub>3</sub>•9H<sub>2</sub>O and Ti(SO<sub>4</sub>)<sub>2</sub> as precursors, respectively.

Fe0.1%T catalyst was also prepared by the homogeneous precipitation method. The aqueous solutions of Fe(NO<sub>3</sub>)<sub>3</sub>•9H<sub>2</sub>O ( $\geq 98.5\%$ ) as Fe precursors and Ti(SO<sub>4</sub>)<sub>2</sub> ( $\geq 96\%$ ) as Ti precursors were mixed with required molar ratios. Excessive urea aqueous solution was then added into the mixed solution. The solution was heated to 90 °C and held there for 12 h under vigorous stir. After filtration and washing with deionized water, the resulting precipitant was dried at 100 °C overnight and subsequently calcined at 400 °C for 6 h in air condition (the heating rate kept at 5 °C/min). The catalyst was signified as Fe0.1%T-h. We also prepared Fe0.1%T catalyst using conventional wet impregnation method for comparison. The precursor was commercial anatase (Degussa). The catalyst was signified as Fe0.1%T-i.

### 2.2. Catalytic measurements

The photocatalytic experiments for the removal of NO were similar to our previous work [38], and are fully described in SI. Briefly, a 500 W commercial xenon arc lamp (Beijing TrusTech Science and Technology Co., China) was used as the light source. Two optical filters were used to obtain light in the 420–700 nm range, and the integrated light intensity was 35.8 mW/cm<sup>2</sup> (FZ-A, radiometer, Photoelectric Instrument Factor of Beijing Normal University). The weight of the photocatalyst used for each experiment was kept at 0.05 g. The initial concentration of NO was diluted to about 400 ppb by the air stream. The desired humidity level of the NO flow was controlled at 55% by passing the nitrogen streams through a humidification chamber. The total flow rate was controlled at 1.2 L min<sup>-1</sup>. The concentration of NO, NO<sub>2</sub> and NO<sub>x</sub> was continuously measured by a chemiluminescence NO<sub>x</sub> analyzer (Thermo Environmental Instruments Inc., Model 42i), which monitors NO, NO<sub>2</sub>, and NO<sub>x</sub> (NO<sub>x</sub> represents NO + NO<sub>2</sub>) with a sampling rate of 0.7 L min<sup>-1</sup>.

In the data analysis, the NO conversion, NO<sub>2</sub> selectivity, and NO<sub>x</sub> conversion were defined as follows:

$$\text{NO conversion} = \frac{[\text{NO}]_{\text{in}} - [\text{NO}]_{\text{out}}}{[\text{NO}]_{\text{in}}}$$

$$\text{NO}_2 \text{ selectivity} = \frac{[\text{NO}_2]_{\text{out}}}{[\text{NO}]_{\text{in}} - [\text{NO}]_{\text{out}}}$$

$$\text{NO}_x \text{ conversion} = \frac{[\text{NO}]_{\text{in}} - [\text{NO}_x]_{\text{out}}}{[\text{NO}]_{\text{in}}}$$

Since NO<sub>2</sub> is more toxic than NO, the photocatalyst performance should be evaluated by the NO<sub>x</sub> conversion, or the NO conversion in conjunction with the NO<sub>2</sub> selectivity.

### 2.3. Catalyst characterization

The actual ratio of Fe in Fe/TiO<sub>2</sub> products was detected using inductively coupled plasma optical emission spectrometer (ICP-OES).

The surface area of the catalyst was determined with a physisorption analyzer (Autosorb-1C-TCD, Quantachrome) by N<sub>2</sub> adsorption-desorption at 77 K. The surface area ( $S_{\text{BET}}$ ) was determined by applying the Brunauer–Emmett–Teller (BET) method to the adsorption isotherm in the partial pressure range of 0.05–0.35.

The crystalline structure of the catalysts was determined by a powder X-ray diffractometer (XRD; X'Pert PRO, PANalytical, Netherlands) using Cu K $\alpha$  ( $\lambda = 0.15406$  nm) radiation at 40 kV and 40 mA. The data of 2 $\theta$  from 20° to 80° were collected at 8°/min with the step size of 0.07°.

Raman spectra of the catalysts were recorded at room temperature on a UV resonance Raman spectrometer (UVR DLPC-DL-03), which consisted of three optional exciting lasers (244, 325, and 532 nm), a three-stage grating spectrograph, and a CCD detector cooled by liquid nitrogen. The instrument was calibrated against the Stokes Raman signal of Teflon at 1378 cm<sup>-1</sup>. A 325-nm He-Cd laser was also used as an exciting source for the measurement of UV Raman. The spectra resolution was 2.0 cm<sup>-1</sup>. All Raman spectra used in the paper were original and unsmoothed.

The UV-vis diffuse reflection spectra of the catalysts over the range of 200–800 nm were recorded at room temperature with a diffuse reflectance UV-vis spectrophotometer (U-3310, Hitachi), using BaSO<sub>4</sub> as reflectance standard.

The photoluminescence (PL) spectra were measured in a home-built laser induced luminescence spectrograph. The photoluminescence signal was collected with an ellipsoidal collecting mirror and focused onto a 320 mm monochromator (Jobin-Yvon Triax 320) by passing through a filter with cutoff wavelength below 360 nm. A charge-coupled device (Jobin-Yvon Spectrum One CCD 3000) was mounted at the focal plane in the exit of the monochromator to detect the luminescence signal. Prior to the experiments, the wavelength calibration of this setup was carried out with a mercury lamp. A 325-nm He-Cd laser was used as the exciting source for the measurement of photoluminescence spectra.

The X-band electron paramagnetic resonance (EPR) spectra were recorded at room temperature using a Bruker A300-10/12 EPR spectrometer.

The XANES of Fe K and Ti K edges were measured in a transmission mode at room temperature on BL-7C beam line, Photon Factory, Institute of Materials Structure Science, High Energy Accelerator Research Organization (IMSS-KEK), Japan. Fe foil, FeO, magnetite Fe<sub>3</sub>O<sub>4</sub> and hematite Fe<sub>2</sub>O<sub>3</sub> were used as reference samples. The storage ring was operated at 2.5 GeV with 300 mA as an average storage current. The synchrotron radiation beam line was monochromatized with a Si (1 1 1) double crystal monochromator,

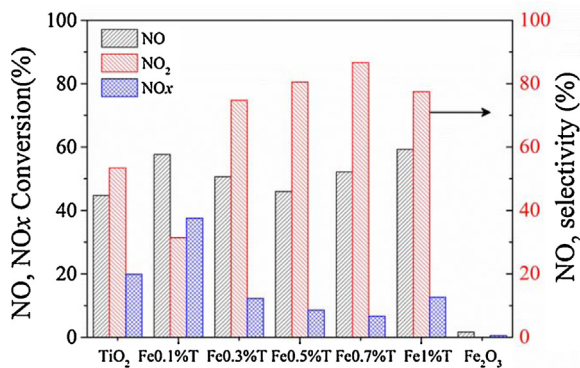


**Fig. 1.** NO conversion, NO<sub>x</sub> conversion and NO<sub>2</sub> selectivity at 0.5 h over Fe<sub>x</sub>%T ( $x=0.1, 0.3, 0.5, 0.7, 1$ ) catalysts and pure oxides including TiO<sub>2</sub> and Fe<sub>2</sub>O<sub>3</sub>.

and mirrors were used to eliminate higher harmonics. The incident and transmitted beam intensities were monitored using ionization chambers filled with pure N<sub>2</sub>. XAFS data were analyzed using the REX2000 program (Rigaku Co.). XANES spectra were normalized with edge height and then taken the first-order derivatives to compare the variation of absorption edge energies.

#### 2.4. DFT calculations

DFT calculations were performed using CASTEP package on the basis of the plane-wave-pseudo-potential approach. The Perdew–Burke–Ernzerhof (PBE) of the generalized gradient approximation (GGA) was used as the exchange–correlation function. The interaction between valence electrons and the ionic core was described by the ultrasoft pseudopotential. Calculations were carried out with a Monkhorst–Pack  $k$ -point mesh of ( $2 \times 2 \times 1$ ) and a plane-wave cutoff of 380 eV.

The initial geometry configurations were optimized by the Broyden, Fletcher, Goldfarb and Shannom (BFGS) minimizer for spin polarized systems with different initial numbers of spin-up and spin-down electrons. The spin occupation numbers were then optimized during the electronic iterations. The energetic convergence threshold for the self-consistent field (SCF) is  $5.0 \times 10^{-7}$  eV/atom. The convergence tolerance parameters of optimized calculations were a maximum energy of  $1.0 \times 10^{-5}$  eV/atom, a maximum force of 0.03 eV/Å, a maximum stress of 0.05 GPa and a maximum displacement of  $1.0 \times 10^{-3}$  Å.

The TiO<sub>2</sub> (101) surfaces were modeled by vacuum slabs. According to previous research [39], we have selected a slab of Ti<sub>48</sub>O<sub>96</sub> with surface area of  $11.09 \times 11.41$  Å<sup>2</sup> (see Fig. S1a), which contained eight O–Ti–O tri-layers (four periodic planes) and was separated by a vacuum gap of 20 Å thicknesses. Thus, the length in each direction

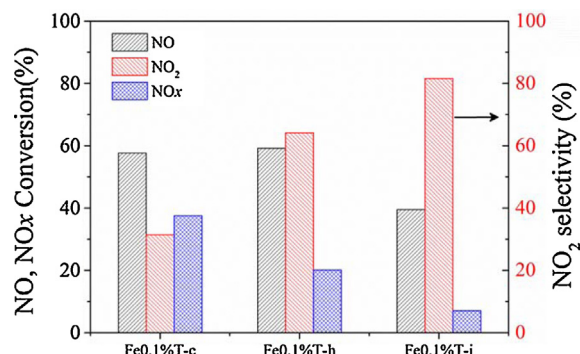


**Fig. 2.** NO conversion, NO<sub>x</sub> conversion and NO<sub>2</sub> selectivity at 0.5 h over Fe0.1%T-c, Fe0.1%T-h and Fe0.1%T-i.

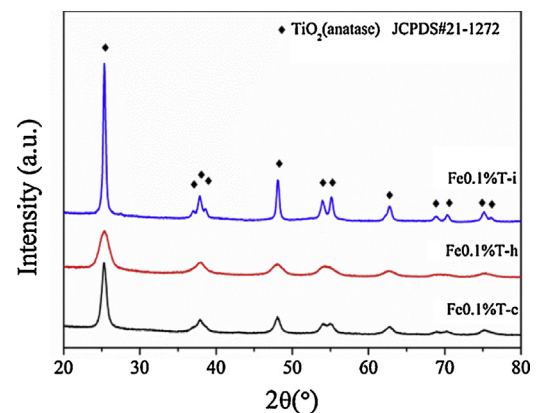


**Fig. 3.** XRD patterns of Fe0.1%T prepared with different methods.

was long enough, so that self-interactions among the impurities could be ignored. The top six tri-layers were relaxed, while the bottom two tri-layers were fixed to mimic the bulk region. The surface sites, namely, the bridging two-fold coordinated oxygen atom (O<sub>2C</sub>), three types of three-fold coordinated oxygen atom (O<sub>3C-1</sub>, O<sub>3C-2</sub>, and O<sub>3C-3</sub>), and five/six-fold coordinated titanium atoms (Ti<sub>5C</sub> and Ti<sub>6C</sub>) are denoted in Fig. S1 as well. According to the experimental results, the model of Fe-doped surface (FeTi<sub>47</sub>O<sub>96</sub>) and Fe on the surface (FeTi<sub>48</sub>O<sub>96</sub>) was built by replacing a surface titanium atom with an iron atom and adding an iron atom at the interstice site on the surface of Ti<sub>48</sub>O<sub>96</sub>, respectively.

The DFT + U method can described the electronic structure, band gaps and defect states of TiO<sub>2</sub> more correctly compare with the DFT method [40,41]. Therefore, after finishing the geometry optimizations, the DFT + U method was used to calculate the band structures and the projected density of states (PDOS) of the models. According to reference [42], the  $U=8.50$  eV of Ti 3d electrons and  $U=5.00$  eV of Fe 3d electrons were adopted in all energy calculation.

### 3. Results and discussion

The reaction of NO with air was negligible when the control experiments were performed with and without light in the absence of a photocatalyst (residence time 5.7 s). Basically, the removal of NO by photocatalysis can be described as follows: NO → HNO<sub>2</sub> → NO<sub>2</sub> → HNO<sub>3</sub>. NO<sub>2</sub> is the intermediate product of this reaction. When the site for the adsorption of HNO<sub>3</sub> is saturated or the concentration of hydroxyl radical is not satisfied to finish the last reaction, NO<sub>2</sub> would release into the air because of desorption. Fig. 1 shows the results of NO conversion, NO<sub>x</sub> conversion, and NO<sub>2</sub> selectivity at 0.5 h for the photocatalytic removal of NO over Fe<sub>x</sub>%T ( $x=0.1, 0.3, 0.5, 0.7, 1$ ) catalysts and pure oxides, including TiO<sub>2</sub> and Fe<sub>2</sub>O<sub>3</sub>. As we can see, pure Fe<sub>2</sub>O<sub>3</sub> showed almost no activity. The conversion of NO was in the range of 45–60% over Fe<sub>x</sub>%T ( $x=0.1, 0.3, 0.5, 0.7, 1$ ) and pure TiO<sub>2</sub>, however, the selectivity of NO<sub>2</sub> (31%) was lowest over Fe0.1%T, and therefore, the conversion of NO<sub>x</sub> (38%) was highest over Fe0.1%T. The activity of Fe0.1%T was two times higher than that of pure TiO<sub>2</sub>. Therefore, we selected Fe0.1%T as the optimal content to carry out further investigations, such as the effects of synthesis methods on photocatalytic NO removal activities, and the relationship between catalyst structure and catalytic activity.

Fig. 2 shows the NO conversion, NO<sub>x</sub> conversion and NO<sub>2</sub> selectivity results at 0.5 h for the photocatalytic removal of NO over Fe0.1%T prepared with different methods. The Fe0.1%T prepared with co-precipitation method (Fe0.1%T-c) showed the highest NO<sub>x</sub> conversion activity. Because the specific areas of the Fe0.1%T prepared with different methods were very different (Table 1), we calculated specific activity normalized by surface area to exclude

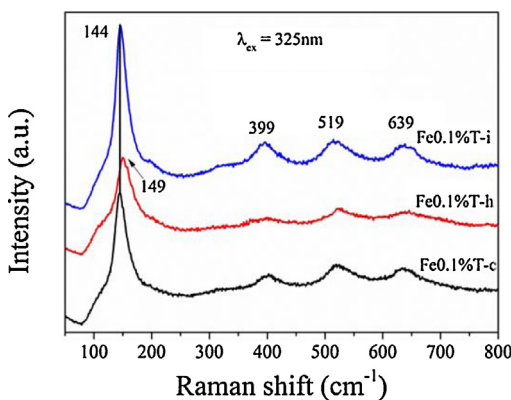


**Fig. 4.** UV Raman spectroscopy of Fe0.1%T prepared with different methods.

the effect of BET surface area on activity (**Table 1**). The specific activity of Fe0.1%T-c was three times higher than that of Fe0.1%T-h and Fe0.1%T-i.

Inductively coupled plasma optical emission spectrometry (ICP-OES) was used to characterize the atomic composition of the catalysts. **Table 1** shows the amount of Fe introduced into the structures as a molar percentage of Fe in relation to the molar percentage of Ti. The molar percentage of Fe was consistent with the initial amount of Fe added, that is 0.11%, 0.10% and 0.12% for Fe0.1%T-c, Fe0.1%T-h and Fe0.1%T-i, respectively.

The crystal structures of Fe0.1%T prepared with different methods were all anatase (JCPDS no.21-1272), as shown by the X-ray diffraction spectra in **Fig. 3**. No other crystalline phase ( $\text{Fe}_2\text{O}_3$  or  $\text{Fe}_x\text{TiO}_y$ ) was observed, which revealed that the Fe content in our samples was below the detection limits of the XRD instrument, or was very finely dispersed over the surface of the particles, or the Fe ions substituted the Ti atoms in the  $\text{TiO}_2$  matrix due to the similar ionic radii of  $\text{Fe}^{3+}$  and  $\text{Ti}^{4+}$  [43].

Raman spectroscopy was used to clearly characterize the  $\text{TiO}_2$  surface structure. The UV Raman spectra of Fe0.1%T prepared with different methods are shown in **Fig. 4**. Raman shifts at 144, 399, 519 and  $639\text{ cm}^{-1}$  attributed to the Raman active modes of anatase with symmetries of  $E_g$ ,  $B_{1g}$ ,  $A_{1g}$  and  $E_g$ , respectively, were observed for all  $\text{TiO}_2$  samples. These results indicate that the surface of Fe0.1%T prepared with different methods were in an anatase state. No  $\text{Fe}_2\text{O}_3$  or other Fe related crystal phases were observed, in agreement with the XRD results.

The  $E_g$  feature of anatase (symmetric stretching vibration of O–Ti–O) at  $144\text{ cm}^{-1}$  was studied in detail. The blue shift in the peak position for the catalyst prepared by homogeneous precipitation method ( $149\text{ cm}^{-1}$ ) compared with the other catalyst ( $144\text{ cm}^{-1}$ ) may be due to the formation of oxygen vacancies or size reduction (phonon quantum confinement model) in  $\text{TiO}_2$  [44,45].

**Fig. 5A** and **B** shows the Fe K-edge X-ray absorption near-edge structures (XANES) of the reference samples, Fe0.1%T-c, Fe0.1%T-h, and Fe0.1%T-i catalysts and their corresponding first-order derivatives, respectively. The first-order derivative peak of the absorption coefficient appeared at 7120.5 eV for  $\text{Fe}^{2+}$  in  $\text{FeO}$ , while that for  $\text{Fe}^{3+}$  in pristine  $\text{Fe}_2\text{O}_3$  appeared at 7127.1 eV. For the three catalysts, the XANES patterns of Fe K edge were different to those of any pristine oxides. This may be due to the low content of Fe and the formation of Fe–O bonds on the surface or the substitution of Ti in the lattice of  $\text{TiO}_2$ . All three catalysts reached a maximum at 7127.1 eV in the first-order derivatives, indicating the presence of  $\text{Fe}^{3+}$  in these catalysts.

**Fig. 5C** and **D** shows the Ti K-edge XANES of  $\text{TiO}_2$ -c, Fe0.1%T-c,  $\text{TiO}_2$ -h, Fe0.1%T-h,  $\text{TiO}_2$  (commercial anatase), Fe0.1%T-i and their corresponding first-order derivatives, respectively. Anatase  $\text{TiO}_2$  was the main crystal phase in all samples and the oxidation state of

**Table 1**  
Specific surface areas and specific activity of Fe0.1%T-c, Fe0.1%T-h and Fe0.1%T-i.

Catalysts	$S_{\text{BET}}$ ( $\text{m}^2 \text{ g}^{-1}$ )	Specific activity (%/ $\text{m}^2/\text{g}$ )	Measured Fe (at%)
Fe0.1%T-c	105.4	0.356	0.11
Fe0.1%T-h	197.3	0.102	0.10
Fe0.1%T-i	68.3	0.103	0.12

Determined using Scherrer's equation (applicable from 3 to 200 nm).

Ti was +4. This was in good agreement with our previous XRD and Raman results. Therefore, from XANES analysis, we confirmed the presence of  $\text{Fe}^{3+}$  in our catalysts, which did not involve any change in the oxidation state of Ti.

Electron paramagnetic resonance (EPR) is a highly sensitive spectroscopic technique for examining paramagnetic species and can give valuable information about the lattice site in which a paramagnetic dopant ion is located. This highly sensitive technique can detect Fe ion levels down to 0.01% in metal oxide matrices [46]. The EPR spectra of Fe0.1%T prepared with different methods are shown in **Fig. 6**. Fe0.1%T-c and Fe0.1%T-h both showed intense signals at  $g=1.99$  and very weak signals at  $g=4.22$ . According to previous reports [47,48], these two signals should be attributed to  $\text{Fe}^{3+}$  substituted for  $\text{Ti}^{4+}$  in the  $\text{TiO}_2$  lattice ( $g=1.99$ ) and to  $\text{Fe}^{3+}$  substituted in the lattice adjacent to a charge-compensating oxide anion vacancy ( $g=4.22$ ), respectively. Analysis of the EPR results confirmed that  $\text{Fe}^{3+}$  ions were successfully incorporated into the crystal lattice of  $\text{TiO}_2$ . The intensity of the EPR signal for Fe0.1%T-c was higher than that for Fe0.1%T-h, which indicated that more  $\text{Fe}^{3+}$  ions were successfully incorporated into the crystal lattice of  $\text{TiO}_2$  prepared by co-precipitation method. The EPR spectra of Fe0.1%T-i showed almost no signals. This suggested that no  $\text{Fe}^{3+}$  ions were incorporated into the crystal lattice of  $\text{TiO}_2$  prepared by conventional wet impregnation method. Therefore,  $\text{Fe}/\text{TiO}_2$  with different Fe states was obtained using different preparation methods.

The optical absorption properties of the Fe0.1%T catalysts were examined with UV-vis diffuse reflectance spectra (DRS) and the results are shown in **Fig. 7**. Fe0.1%T-i had weak absorption in the visible light region ( $>400\text{ nm}$ ), whereas Fe0.1%T-c and Fe0.1%T-h exhibited red shifts of the absorption edge and a significant enhancement of light absorption at wavelengths of 400–600 nm. The band gap energies of Fe0.1%T-i, Fe0.1%T-h and Fe0.1%T-c were calculated to be 3.27, 3.13 and 2.93 eV, respectively. The narrowing of the band gap effectively improved the photocatalytic activity in the visible-light region. According to previous reports [47,49], the presence of metal ions in  $\text{TiO}_2$  does not modify the position of the valence band edge of  $\text{TiO}_2$ . Instead, it introduces new energy levels ( $\text{Fe}^{2+}/\text{Fe}^{3+}$ ) of the transition metal ions into the band gap of  $\text{TiO}_2$ . Therefore, the absorption edges shifts toward longer wavelengths for  $\text{Fe}/\text{TiO}_2$  should come from the electronic transition from the dopant energy level ( $\text{Fe}^{2+}/\text{Fe}^{3+}$ ) to the conduction band of  $\text{TiO}_2$ .

During the photocatalytic process, charge transfer and recombination are two competing reaction pathways. It is important to suppress the recombination rate and accelerate charge transfer to enhance photocatalytic activity. Photoluminescence (PL) emission spectra can be used to understand the fate of photo-generated electrons and holes in semiconductor particles since PL emission results from the recombination of free carriers [50,51].

The PL emission spectra of the catalysts are shown in **Fig. 8**, which reveal nearly identical peaks in shape and position for all catalysts. The PL intensity of Fe0.1%T-c was much lower than that of Fe0.1%T-h and Fe0.1%T-i, indicating that electron–hole recombination on the surface of Fe0.1%T-c was largely inhibited to generating more photoelectrons and holes to participate in the photocatalytic reaction. The reason is that  $\text{Fe}^{3+}$  incorporated into the  $\text{TiO}_2$  lattice can act as an electron-trapped agent to promote electron–hole separation [52].

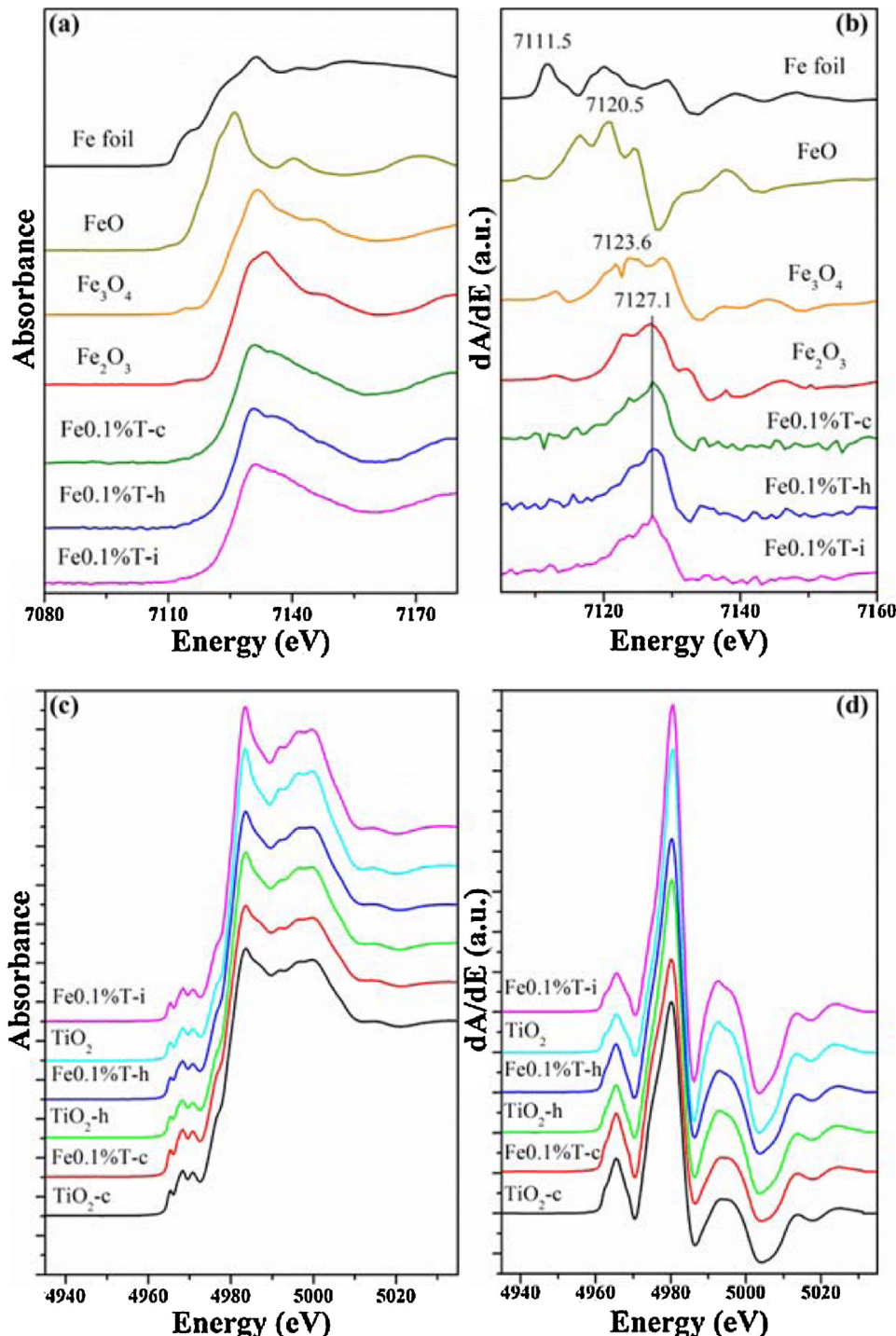


**Fig. 5.** (a) Fe K-edge XANES, (b) first-order derivatives of Fe K-edge XANES, (c) Ti K-edge XANES and (d) first-order derivatives of Ti K-edge XANES in different samples.

Based on the experimental characterization results, we performed theoretical calculations to gain a deeper understanding of the effect of Fe doping on the structural and electronic properties of the catalysts.

Anatase has a tetragonal crystal structure with space group I41/AMD (141). The calculated lattice parameters of the pure  $\text{TiO}_2$  model were  $a=b=3.803 \text{ \AA}$  and  $c=9.695 \text{ \AA}$  at ambient conditions, which were in good agreement with the previous experiment values of  $a=b=3.782 \text{ \AA}$  and  $c=9.502 \text{ \AA}$  [53]. When  $U=8.5 \text{ eV}$  for the Ti 3d electrons was adopted in energy calculations, the calculated band gap of pure anatase  $\text{TiO}_2$  was 3.26 eV, which was in

agreement with our experimental values and previous research [42]. Because (101) is the majority exposed facets of anatase, we optimized the structure of the perfect  $\text{TiO}_2$  (101) surface (Fig. 9(a)). The most important outward relaxations were those of  $\text{O}_{3\text{C}-1}$  and  $\text{Ti}_{6\text{C}}$  atoms ( $0.19$  and  $0.23 \text{ \AA}$ , respectively), while the  $\text{Ti}_{5\text{C}}$  atoms moved inward by  $-0.14 \text{ \AA}$ . Therefore, the  $\text{O}_{3\text{C}-1}$  atoms were located above the  $\text{Ti}_{5\text{C}}$  atoms on the relaxed surface, as shown in Fig. S1. The surface configuration was consistent with previous reports [54–57], indicating that our calculation methods and results were reasonable and valid. Based on the results, we construct a Fe-doped surface model ( $\text{FeTi}_{47}\text{O}_{96}$ ) and Fe on the surface model ( $\text{FeTi}_{48}\text{O}_{96}$ )

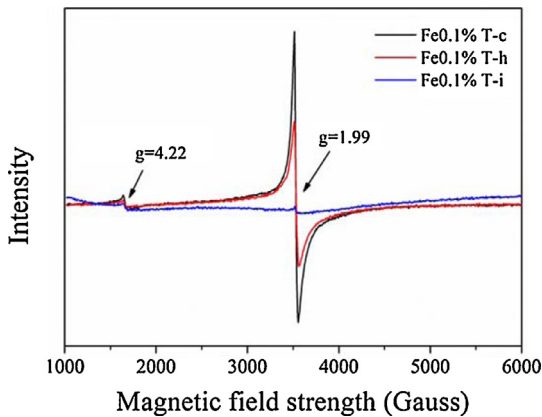


**Fig. 6.** ESR spectra of Fe0.1%T prepared with different methods.

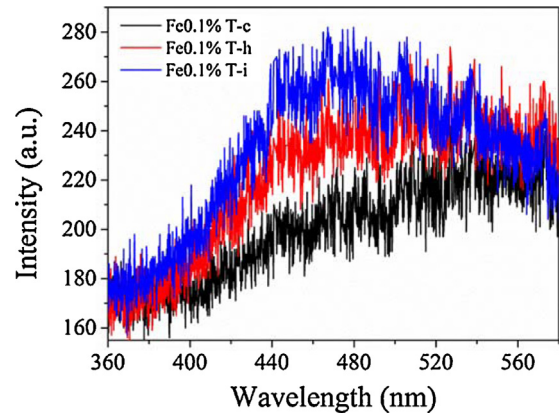


**Fig. 8.** Photoluminescence (PL) emission spectra of the catalysts.

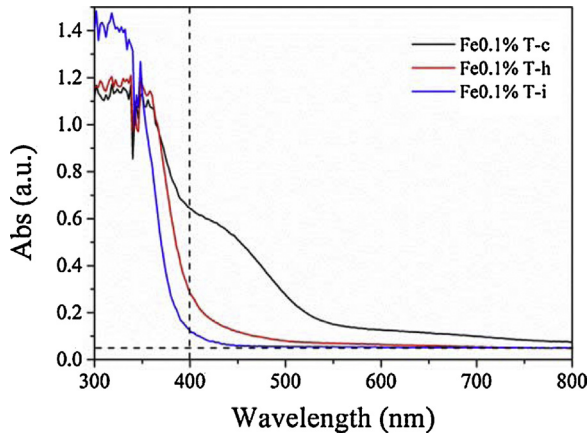


**Fig. 7.** UV-vis diffuse reflectance spectra of Fe0.1%T prepared with different methods.

representing the catalysts prepared by co-precipitation method and conventional wet impregnation method, respectively.

For the Fe-doped surface ( $\text{FeTi}_{47}\text{O}_{96}$ ) model, there were two possible surface sites ( $\text{Ti}_{5\text{C}}$  and  $\text{Ti}_{6\text{C}}$ ) for Fe atom substitution. Comparing the total energies of the two possible optimized configurations of the Fe-doped surface ( $\text{FeTi}_{47}\text{O}_{96}$ ) model indicated that the  $\text{Ti}_{5\text{C}}$  site was energetically favored. Fig. 9(b) exhibits the relaxed configuration of a Fe atom substituting a Ti atom at the  $\text{Ti}_{5\text{C}}$  site. The substitution Fe atom was connected to neighboring O atoms and the optimized Fe–O bond lengths were 1.972, 1.898, 1.971, 1.907 and 1.758 Å. Compared with the original Ti–O bond lengths (1.986, 2.067, 1.987, 1.781 and 1.832 Å) of the  $\text{Ti}_{48}\text{O}_{96}$  surface model (Fig. 9(a)), the substitution of Fe atom for Ti atom did not lead to significant lattice distortion. For the Fe on the surface ( $\text{FeTi}_{48}\text{O}_{96}$ ), the energetically favored model is shown in Fig. 9(c). After optimization, the lengths of the Ti–O bonds nearest the Fe atom were 2.112, 1.887, 2.029, 2.026, 1.886, 2.115, 2.003 and 2.003 Å. Compared with

the original Ti–O bond lengths (1.8662, 1.832, 1.987, 1.986, 1.832, 1.862, 1.943 and 1.942 Å) of the  $\text{Ti}_{48}\text{O}_{96}$  surface model (Fig. 9(a)), the Fe atom added on the surface of the  $\text{Ti}_{48}\text{O}_{96}$  model did not lead to significant lattice distortion.

The band structures of the  $\text{Ti}_{48}\text{O}_{96}$ ,  $\text{FeTi}_{47}\text{O}_{96}$  and  $\text{FeTi}_{48}\text{O}_{96}$  surface models were obtained by the DFT + U calculations, as shown in Fig. S2. The calculated band gaps were 2.59, 1.61 and 2.53 eV for the  $\text{Ti}_{48}\text{O}_{96}$ ,  $\text{FeTi}_{47}\text{O}_{96}$  and  $\text{FeTi}_{48}\text{O}_{96}$  surface models, respectively. This indicated that the substitution of Fe atom for Ti atoms lead to a narrowing of the band gap, which was consistent with the experimental results (Fig. 7).

To understand the origin of the band gap variation, total density of states (DOS) and projected density of states (PDOS) were calculated and plotted in Fig. 10, with up-spin DOS above zero and down-spin DOS below zero. For the pure surface  $\text{Ti}_{48}\text{O}_{96}$  model (Fig. 10(a)), the valence band (VB) consisted of Ti 3d and O 2p states, and the conductive band (CB) primarily consisted of Ti 3d states, which was consistent with previous studies [39,42]. For the  $\text{FeTi}_{47}\text{O}_{96}$  model, the Fe 3d states were located at the bottom of the CB and partially overlapped with the energy band of  $\text{TiO}_2$ , as shallow donor energy levels. According to Fig. 10(b), Fe doping also induced an acceptor state at the top of the VB as shallow acceptor energy levels, which was caused by hybridization between the Fe 3d, O 2p and Ti 3d states. Therefore, these impurity states prolonged the lifetimes of photoexcited carriers and enhanced photocatalytic performance. For the  $\text{FeTi}_{48}\text{O}_{96}$  model, the Fe 3d states were located at the bottom of the VB and overlapped with the VB of  $\text{TiO}_2$ . Two spin-parallel electronic levels were located at 1.08 and 1.54 eV from the top of the VB, as shown in Fig. 10(c). The location of the two levels suggested a deep donor level and accelerated recombination of photoexcited electron and holes. The calculated results indicated that the electronic structure of  $\text{TiO}_2$  was changed by the Fe atom.

Experimental characterization demonstrated that Fe ions incorporated into the crystal lattice of  $\text{TiO}_2$  narrow the band gap of the catalysts, enhance the visible light absorption and improve the separation efficiency of electron hole pairs. Theoretical calculations

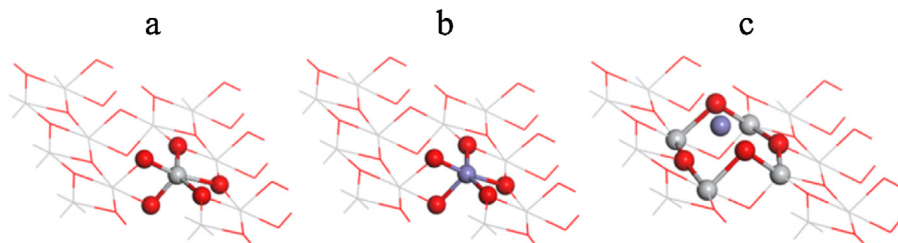


**Fig. 9.** Relaxed structure of the first layer of (a)  $\text{Ti}_{48}\text{O}_{96}$ , (b)  $\text{FeTi}_{47}\text{O}_{96}$  and (c)  $\text{FeTi}_{48}\text{O}_{96}$ .

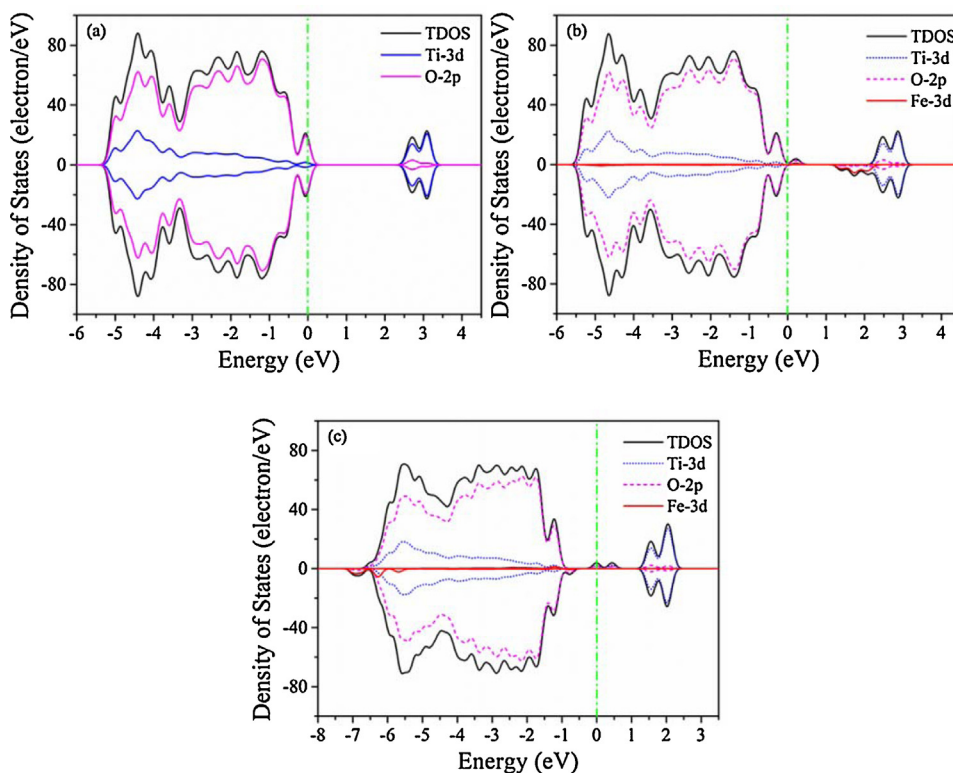


**Fig. 10.** The DFT+U density of states for (a)  $\text{Ti}_{48}\text{O}_{96}$ , (b)  $\text{FeTi}_{47}\text{O}_{96}$  and (c)  $\text{FeTi}_{48}\text{O}_{96}$ . The energy zero is taken as the Fermi level and displayed with a green dashed line.

showed that the model of Fe incorporated into the crystal lattice of  $\text{TiO}_2$  had the narrower band gap and shallow acceptor levels to promote the separation of electron and hole in the band gap. The theoretical calculation results verified the experimental characterization results, and indicated that the importance of Fe replaces the Ti in the  $\text{TiO}_2$  lattice for the enhancement of the photocatalytic activity.

#### 4. Conclusions

The present study demonstrated the importance of Fe ions incorporated into the crystal lattice of  $\text{TiO}_2$ . The incorporated Fe ions substituted the octahedrally coordinated  $\text{Ti}^{4+}$  ions in the  $\text{TiO}_2$  lattice, which extended the visible light absorption; and hence, promoted the formation of electron–hole pairs. Furthermore, the doping of Fe increased the electron–hole separation efficiency because  $\text{Fe}^{3+}$  incorporated into  $\text{TiO}_2$  can act as an electron-trapped agent. Fe ions substituted the Ti ions of  $\text{TiO}_2$  prepared by the co-precipitation method, however, no Fe ions were incorporated into the crystal lattice of the  $\text{TiO}_2$  prepared by the conventional wet impregnation method. The structural differences caused by different preparation method determined the photocatalytic activity of  $\text{Fe}/\text{TiO}_2$ .

#### Acknowledgments

This work was supported by the Strategic Priority Research Program of the Chinese Academy of Sciences (XDB05050600) and the National Natural Science Foundation of China (21207145, 51221892).

#### Appendix A. Supplementary data

Supplementary data associated with this article can be found, in the online version, at <http://dx.doi.org/10.1016/j.apcatb.2015.05.003>.

#### References

- [1] B. Zhao, S.X. Wang, H. Liu, J.Y. Xu, K. Fu, Z. Klimont, J.M. Hao, K.B. He, J. Cofala, M. Amann, *Atmos. Chem. Phys.* 13 (2013) 9869–9897.
- [2] H. He, Y.S. Wang, Q.X. Ma, J.Z. Ma, B.W. Chu, D.S. Ji, G.Q. Tang, C. Liu, H.X. Zhang, J.M. Hao, *Sci. Rep.* 4 (2014) 4172.
- [3] Z.H. Ai, W.K. Ho, S.C. Lee, *J. Phys. Chem. C* 115 (2011) 25330–25337.
- [4] F. Dong, Y.J. Sun, M. Fu, W.-K. Ho, S.C. Lee, Z.B. Wu, *Langmuir* 28 (2012) 766–773.
- [5] H. Yamashita, K. Yoshizawa, M. Ariyuki, S. Higashimoto, M. Che, M. Anpo, *Chem. Commun.* (2001) 435–436.
- [6] J.L. Zhang, T. Ayusawa, M. Minagawa, K. Kinugawa, H. Yamashita, M. Matsuoka, M. Anpo, *J. Catal.* 198 (2001) 1–8.
- [7] J.L. Zhang, Y. Hu, M. Matsuoka, H. Yamashita, M. Minagawa, H. Hidaka, M. Anpo, *J. Phys. Chem. B* 105 (2001) 8395–8398.
- [8] F. Dong, Y. Huang, S.C. Zou, J.A. Liu, S.C. Lee, *J. Phys. Chem. C* 115 (2011) 241–247.
- [9] G. Dong, W. Ho, L. Zhang, *Appl. Catal. B* 168–169 (2015) 490–496.
- [10] F. Dong, Z. Wang, Y. Li, W.-K. Ho, S.C. Lee, *Environ. Sci. Technol.* 48 (2014) 10345–10353.
- [11] F. Dong, Q. Li, Y. Sun, W.-K. Ho, *ACS Catal.* 4 (2014) 4341–4350.
- [12] K.-C. Huang, S.-H. Chien, *Appl. Catal. B* 140–141 (2013) 283–288.
- [13] A.V. Katsanaki, A.G. Kontos, T. Maggos, M. Pelaez, V. Likodimos, E.A. Pavlatou, D.D. Dionysiou, P. Falaras, *Appl. Catal. B* 140–141 (2013) 619–625.
- [14] A. Fujishima, K. Honda, *Nature* 238 (1972) 37–38.
- [15] R. Long, *J. Phys. Chem. Lett.* 4 (2013) 1340–1346.
- [16] Z.H. Ai, W.K. Ho, S.C. Lee, L.Z. Zhang, *Environ. Sci. Technol.* 43 (2009) 4143–4150.
- [17] D.J. Yang, C.C. Chen, Z.F. Zheng, H.W. Liu, E.R. Waclawik, Z.M. Yan, Y.N. Huang, H.J. Zhang, J.C. Zhao, H.Y. Zhu, *Energy Environ. Sci.* 4 (2011) 2279–2287.
- [18] C. Gionco, M.C. Paganini, E. Giannello, R. Burgess, C. Di Valentini, G. Pacchioni, *J. Phys. Chem. Lett.* 5 (2014) 447–451.
- [19] J.M. Valero, S. Obregón, G. Colón, *ACS Catal.* 4 (2014) 3320–3329.
- [20] J.C. Yu, J.G. Yu, W.K. Ho, Z.T. Jiang, L.Z. Zhang, *Chem. Mater.* 14 (2002) 3808–3816.
- [21] Y.W. Wang, L.Z. Zhang, S. Li, P. Jena, *J. Phys. Chem. C* 113 (2009) 9210–9217.
- [22] A. Du, Y.H. Ng, N.J. Bell, Z. Zhu, R. Amal, S.C. Smith, *J. Phys. Chem. Lett.* 2 (2011) 894–899.
- [23] C. Barzan, E. Groppo, S. Bordiga, A. Zecchina, *ACS Catal.* 4 (2014) 986–989.
- [24] X. Yu, B. Kim, Y.K. Kim, *ACS Catal.* 3 (2013) 2479–2486.
- [25] X.B. Chen, L. Liu, P.Y. Yu, S.S. Mao, *Science* 331 (2011) 746–750.
- [26] F. Dong, H.Q. Wang, Z.B. Wu, *J. Phys. Chem. C* 113 (2009) 16717–16723.
- [27] F. Dong, S. Guo, H.Q. Wang, X.F. Li, Z.B. Wu, *J. Phys. Chem. C* 115 (2011) 13285–13292.

- [28] M. Liu, X.Q. Qiu, M. Miyauchi, K. Hashimoto, *J. Am. Chem. Soc.* 135 (2013) 10064–10072.
- [29] H.G. Yu, H. Irie, Y. Shimodaira, Y. Hosogi, Y. Kuroda, M. Miyauchi, K. Hashimoto, *J. Phys. Chem. C* 114 (2010) 16481–16487.
- [30] Q.P. Wu, R. van de Krol, *J. Am. Chem. Soc.* 134 (2012) 9369–9375.
- [31] S. George, S. Pokhrel, Z.X. Ji, B.L. Henderson, T. Xia, L.J. Li, J.I. Zink, A.E. Nel, L. Madler, *J. Am. Chem. Soc.* 133 (2011) 11270–11278.
- [32] C. Chen, X. Li, W. Ma, J. Zhao, H. Hidaka, N. Serpone, *J. Phys. Chem. B* 106 (2001) 318–324.
- [33] J.G. Yu, Q.J. Xiang, M.H. Zhou, *Appl. Catal. B* 90 (2009) 595–602.
- [34] J. Choi, H. Park, M.R. Hoffmann, *J. Phys. Chem. C* 114 (2009) 783–792.
- [35] F.M. Dukes, E. Iuppa, B. Meyer, M.J. Shultz, *Langmuir* 28 (2012) 16933–16940.
- [36] J. Navío, G. Colón, M.I. Litter, G.N. Bianco, *J. Mol. Catal. A* 106 (1996) 267–276.
- [37] L.P. Wen, B.S. Liu, X.J. Zhao, K. Nakata, T. Murakami, A. Fujishima, *Int. J. Photoenergy* 2012 (2012) 368750.
- [38] J.Z. Ma, H.M. Wu, Y.C. Liu, H. He, *J. Phys. Chem. C* 118 (2014) 7434–7441.
- [39] Z.Y. Zhao, Z.S. Li, Z.G. Zou, *ChemPhysChem* 13 (2012) 3836–3847.
- [40] B.J. Morgan, G.W. Watson, *J. Phys. Chem. C* 113 (2009) 7322–7328.
- [41] G.S. Shao, *J. Phys. Chem. C* 113 (2009) 6800–6808.
- [42] Q.L. Chen, B. Li, G. Zheng, K.H. He, A.S. Zheng, *Physica B: Condens. Matter* 406 (2011) 3841–3846.
- [43] C.Y. Wang, C. Bottcher, D.W. Bahnemann, J.K. Dohrmann, *J. Mater. Chem.* 13 (2003) 2322–2329.
- [44] A. Li Bassi, D. Cattaneo, V. Russo, C.E. Bottani, E. Barborini, T. Mazza, P. Pisari, P. Milani, F.O. Ernst, K. Wegner, S.E. Pratsinis, *J. Appl. Phys.* 98 (2005) 074305.
- [45] J.C. Parker, R.W. Siegel, *J. Mater. Res.* 5 (1990) 1246–1252.
- [46] T.A. Egerton, E. Harris, E.J. Lawson, B. Mile, C.C. Rowlands, *Phys. Chem. Chem. Phys.* 3 (2001) 497–504.
- [47] K. Nagaveni, M.S. Hegde, G. Madras, *J. Phys. Chem. B* 108 (2004) 20204–20212.
- [48] M. Graetzel, R.F. Howe, *J. Phys. Chem.* 94 (1990) 2566–2572.
- [49] W. Choi, A. Termin, M.R. Hoffmann, *J. Phys. Chem.* 98 (1994) 13669–13679.
- [50] Y. Yu, J.C. Yu, C.Y. Chan, Y.K. Che, J.C. Zhao, L. Ding, W.K. Ge, P.-K. Wong, *Appl. Catal. B* 61 (2005) 1–11.
- [51] Q.J. Xiang, K.L. Lv, J.G. Yu, *Appl. Catal. B* 96 (2010) 557–564.
- [52] S. Sun, J.J. Ding, J. Bao, C. Gao, Z.M. Qi, X.Y. Yang, B. He, C.X. Li, *Appl. Surf. Sci.* 258 (2012) 5031–5037.
- [53] J.K. Burdett, T. Hugbanks, G.J. Miller, J.W. Richardson, J.V. Smith, *J. Am. Chem. Soc.* 109 (1987) 3639–3646.
- [54] Z.Y. Zhao, Z.S. Li, Z.G. Zou, *J. Phys. Condens. Matter* 22 (2010) 175008.
- [55] Q. Chen, C. Tang, G. Zheng, *Physica B: Condens. Matter* 404 (2009) 1074–1078.
- [56] Y. Xu, W.-K. Chen, S.-H. Liu, M.-J. Cao, J.-Q. Li, *Chem. Phys.* 331 (2007) 275–282.
- [57] M. Lazzari, A. Vittadini, A. Selloni, *Phys. Rev. B* 63 (2001) 155409.